



# Review on thermoelectrical properties of selected imines in neat and multicomponent layers towards organic opto-electronics and photovoltaics

K. A. Bogdanowicz<sup>\*</sup> , A. Iwan 

Military Institute of Engineer Technology, 136 Obornicka St., 50-961 Wrocław, Poland

## Article info

### Article history:

Received 21 Nov. 2021

Received in revised form 07 Dec. 2021

Accepted 08 Dec. 2021

Available on-line: 27 Dec. 2021

### Keywords:

Chronoamperometry, CSA, imines, PC<sub>71</sub>BM, PTB7, thermal imaging camera, thermoelectrical properties.

## Abstract

The present review is mainly focused on the extended analysis of the results obtained from coupled measurement techniques of a thermal imaging camera and chronoamperometry for imines in undoped and doped states. This coupled technique allows to identify the current-voltage characteristics of thin films based on imine, as well as to assess layer defects in thermal images. Additional analysis of results provides further information regarding sample parameters, such as resistance, conductivity, thermal resistance, and Joule power heat correlated with increasing temperature. As can be concluded from this review, it is possible not only to study material properties at the supramolecular level, but also to tune macroscopic properties of  $\pi$ -conjugated systems. A detailed study of the structure-thermoelectrical properties in a series of eight unsymmetrical and symmetrical imines for the field of optoelectronics and photovoltaics has been undertaken. Apart from this molecular engineering, the imines properties were also tuned by supramolecular engineering via protonation with camphorsulfonic acid and by creation of bulk-heterojunction compositions based on poly(4,8-bis[(2-ethylhexyl)oxy]benzo[1,2-b:4,5-b']dithiophene-2,6-diyl-alt-3-fluoro-2-[(2-ethylhexyl)carbonyl]thieno[3,4-b]thiophene-4,6-diyl) and/or [6,6]-phenyl-C71-butyric acid methyl ester, poly(3,4-ethylenedioxythiophene) towards the analysed donor or acceptor ability of imines in the active layer. The use of coupled measurement techniques of a thermal imaging camera and chronoamperometry allows obtaining comprehensive data on thermoelectric properties and defects indicating possible molecule rearrangement within the layer.

## 1. Introduction

In recent years, semiconducting organic materials have drawn attention as candidates for numerous applications not only because of their good flexibility and solution processability, but also for their low thermal conductivity and prominent thermoelectric properties at room temperature, large-area processing, flexibility [1,2]. These characteristics respond to the growing demand for distributed energy in new, emerging fields, like power generation, sensing devices or internet of things (IoT) [3].

Production of large surface area organic solar cells is essential to ensure an adequate level of efficiency in the conversion of solar radiation to electricity, in order to replace standard fossil fuels. For large surface area organic solar cells, the energy conversion efficiency is still low; a thin active layer responsible to the greatest extent for the process of transforming one type of energy into another is thin (approx. 100–300 nm) and prone to leakage current, which is the result of layer defects. Defect identification and testing is, therefore, a significant problem, the solution of which will significantly improve the functioning of devices such as organic solar cells [4].

<sup>\*</sup>Corresponding author at: [bogdanowicz@witi.wroc.pl](mailto:bogdanowicz@witi.wroc.pl)

<https://doi.org/10.24425/opelre.2021.139754>

1896-3757/ Association of Polish Electrical Engineers (SEP) and Polish Academic of Sciences (PAS). Published by PAS

© 2021 The Author(s). This is an open access article under the CC BY license (<http://creativecommons.org/licenses/by/4.0/>).

The principle of operation of an organic solar cell is based on a four-step conversion of the incident solar radiation into electric current (Fig. 1). In the system, the active layer of the cell consists of a part carrying the hole in contact with the anode and an acceptor which is a material transporting electrons to the cathode. In the first stage, after the photon absorption, an excited state, an exciton is created. In the second stage, the charges at the donor/acceptor interface are separated, which are dissociated into a positive charge (holes) and negative charges (electrons) between the donor and acceptor, which is the third stage. In the fourth stage, negative charges are transported through the acceptor layer to the cathode, while positive charges are transported through the donor layer to the anode [5].

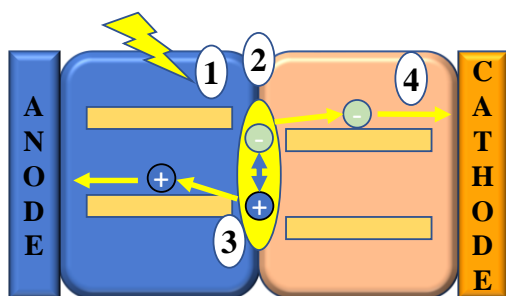


**Fig.1.** Diagram of the processes taking place in an organic solar cell, where 1 represents the absorption of a photon of light; 2 represents the charge separation in acceptor/donor interface; 3 is the charge dissociation between acceptor and donor; 4 is the charge transportation through layers.

All these processes require from organic layers an appropriate charge conduction observed as electric current. Heat is generated as a side effect according to the Joule's law. Both phenomena can be used to study and analyse structural defects of the organic solar cell active layers, similarly to the fourth stage of the processes taking place in the active layer during its operation. In order to study the thermal behaviour of samples, a thermographic camera comes as a suitable solution. The possibility of using thermal imaging has been widely used in aerial thermography [6], aerospace industry [7], automotive industry [8], chemical [9], electrical and electronical industry [10], material testing [11], and security [12]. However, in the field of solar cells the thermal imaging is mainly used to evaluate the system efficiency losses on a photovoltaic installation to determine the actual health status [13–15]. It was noticed that a full description can be obtained by coupling the thermal and electric signatures of the system to acquire a whole description of the working installation [16].

Only recently, coupled techniques based on thermal imaging and chronoamperometry were first used by our team to study structural defects of components for flexible electrodes based on L,D-poly lactide or Ecoflex® containing reduced graphene oxide, single-walled carbon nanotubes, and other additives [17–20]. The results confirmed the usefulness of these coupled techniques to demonstrate structural homogeneity, defects of casted layers, damages done by mechanical stress, or thermal degradation. One attempt was also made to investigate the complex layered structure of a real organic solar cell with architecture of glass/indium tin oxide

(ITO)/TiO<sub>2</sub>/AZJ1(imine)/Au, however, the results showed no characteristic result, allowing the identification of defects in the specific layers [21].

Another part of an organic solar cell that was investigated to increase understanding of the cell specific elements was the active layer. Several articles have been published describing the thermoelectric behaviour of different composition active layers based on imine compounds with triphenylamine [22–25] or terthiophene units [22,26,27].

Finally, inspired by the above-described findings, a detailed study of the structure and thermoelectric properties in a series of 8 unsymmetrical and symmetrical imines (see Fig. 2) for the field of optoelectronics and photovoltaics has been undertaken. Apart from this molecular engineering, the imines properties were also tuned by supramolecular engineering via protonation with camphorsulfonic acid (CSA) and by creation of bulk-heterojunction compositions based on poly(4,8-bis[(2-ethylhexyl)oxy]benzo[1,2-b:4,5-b']dithiophene-2,6-diyl-alt-3-fluoro-2-[(2-ethylhexyl)carbonyl]thieno[3,4-b]thiophene-4,6-diyl) (PTB7) and/or [6,6]-phenyl-C71-butyric acid methyl ester, poly(3,4-ethylenedioxythiophene) (PC<sub>71</sub>BM) towards the analysed donor or acceptor ability of imines in the active layer. Additionally, based on the described results, a further analysis is presented consisting of the influence of the sample temperature on current flow, resistance, conductivity, thermal resistance, and Joule power heat.

To the best of our knowledge, it is the first review paper where similarities and differences between undoped and doped imines are analysed in detail by thermal imaging-chronoamperometry towards photovoltaic applications.

It should be mentioned that many scientists now believe that the synthesized compounds with a charge-transfer function are ones of the most important molecular materials that are functionalized by electron-donating (D) and electron-accepting (A) groups through a  $\pi$ -conjugated link. These are, for example, compounds containing groups of the type: D- $\pi$ -A, D- $\pi$ -D, A- $\pi$ -A, and D- $\pi$ -A- $\pi$ -D or A- $\pi$ -D- $\pi$ -A with different length of chain conjugation and strength of donor and acceptor in the molecule, such as hyperbranched polymers [28], two-photon dyes [29–32], trivalent boron derivatives [33], heterocycle dyes [34] and azomethines [35–37].

Taking into consideration potential applications of the investigated molecules, the compounds with D- $\pi$ -A structures have aroused great interest in technological research. In the presented review, this point of view has been verified by use of thermal imaging-chronoamperometry of selected unsymmetrical and symmetrical imines. By modifying the donors and/or acceptors, the materials properties can be easily changed.

## 2. Thermal imaging-chronoamperometry using the coupled technique

Coupled techniques were designed to complement and correlate test results using at least two different techniques. In the case of the thin film analysis for solar cells, a combination of thermal imaging measurement techniques and chronoamperometry was used. The purpose of using

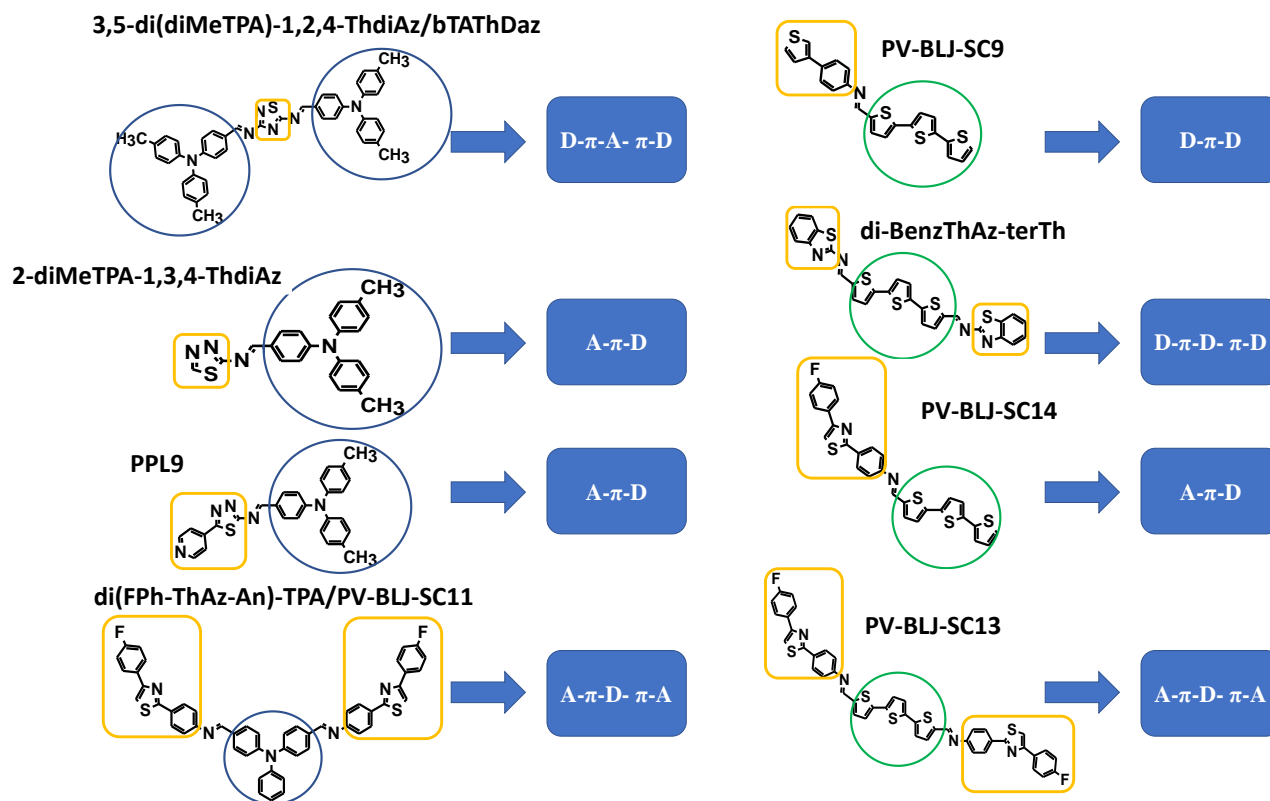


Fig. 2. Chemical structures of the investigated imines.

both techniques in a coupled system is to obtain information on the temperature evolution and distribution with different voltage parameters for a thin layer during a forced current flow. The experiment is modulated by increasing the external potential at 3-minute intervals. This design of the procedure allows the current flow and the sample temperature to be stabilized during each step (Fig. 3) [21].

The measuring setup stand consists of a VIGOCam V50 thermal imaging camera (VIGO System S.A., Poland) and a multi-channel PGstat Autolab M101 potentiostat-galvanostat (Metrohm, the Netherlands) controlled by computer software to synchronize individual procedure stages.

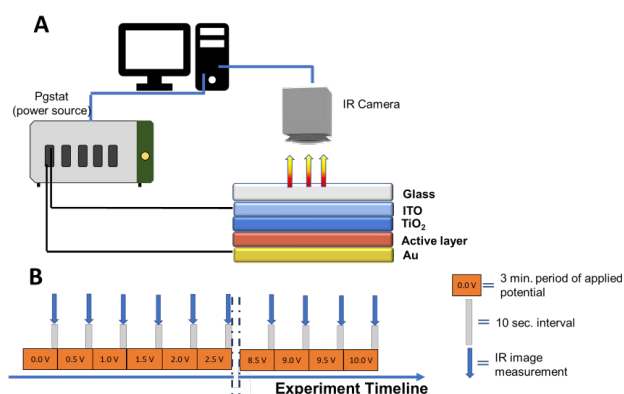


Fig. 3. Thermography setup used to record images at different potentials (a), experimental timeline visualization presenting steps during thermographic experiment (b). Reproduced from Ref. 20 with permission.

As a result of the test, three types of different results answers are obtained:

- information on the type of conductivity,
- information on the maximum obtained temperature,
- map of the thermal image of the tested object.

The type of conductivity is determined by a graphical representation of dependence between the current flow in relation to a given potential. The data allows to determine the layer resistance and sample conductivity.

The maximum temperature of the sample informs indirectly about the thermal conductivity of the sample, accordingly to the Joule's law. Since the method of recording the thermal imaging takes place at the end of a 3-minute stabilization period, a constant current flow is maintained through the sample.

The thermal map allows for determination of individual areas of heating with the possibility of determining the homogeneity of the sample in terms of the heat distribution.

The samples are prepared for testing by a spin coating technique, spreading the solution of active compounds with a total concentration of 15 mg/mL. The speed, in which the layer forms, was usually of 5000 rpm for 20 s giving a layer of approximately 40 nm thick. Of course, in some cases other speeds, e.g., 900 rpm can be used to simulate the actual thickness of an active layer in a solar cell.

### 3. Thermoelectric properties of selected neat imines

For this review, eight imines with different molecular structures were selected as is presented in Fig. 2. From

structural point of view, these compounds can be divided into two major groups containing triphenylamine (2-diMeTPA-1,3,4-ThdiAz, 3,5-(diMeTAP)-1,2,4-thdiAz, PPL9, and di(FPh-ThAz-An)-TPA) or terthiophene (di-BenzThAz-terTh, PV-BLJ-SC9, PV-BLJ-SC13, and PV-BLJ-SC14) groups, showing also symmetry or its lack. Selected properties of these imines can be found in Table 1. Details about synthesis and characterization of the selected imines with triphenylamine [22–25] or terthiophene units [22,26,27] can be found in our previously cited papers.

As mentioned in the previous section, the chronoamperometry techniques of the coupled thermal imaging camera provide basic information regarding the current-

voltage values and the thermal effect of the passing current flow. A system consisting of a glass substrate with a conductive indium tin oxide (ITO) layer and an active layer made of imine was prepared for the study, giving the cell architecture of ITO/active layer/Ag/ITO.

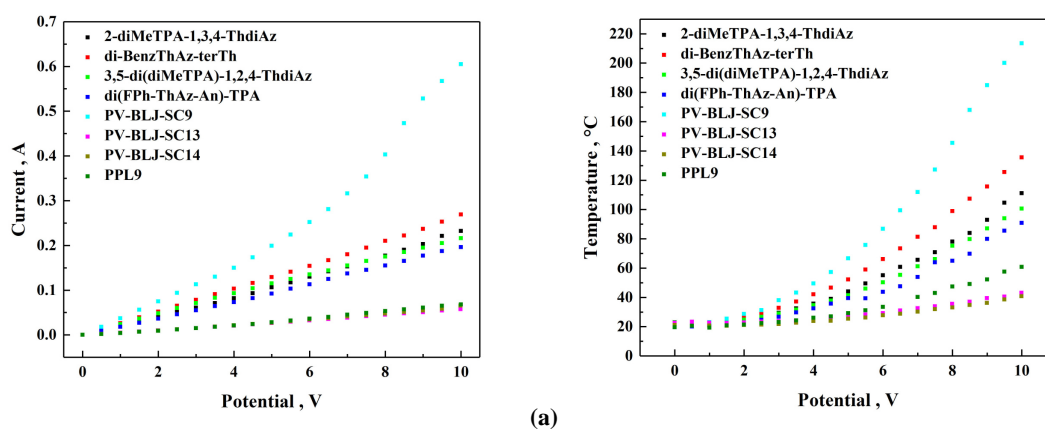
The V-I graphs presented in Refs. 22–27 showed how the value of the current section end-value changed for a given voltage [Fig. 4(a), right]. Within each section the current flow was mostly stable which suggested that no degradation or immense arrangement occurred.

When looking at changes in the maximum value of the sample temperature in relation to the applied voltage, the temperature values increased almost logarithmically

Table 1.  
Summary of spectral, electrochemical, electrical and thermal properties of selected imines.

Code	spin speed, [rpm]	$\lambda_{\max}$ (UV-Vis) [nm]	$\lambda_{\text{offset}}$ [nm]	HOMO [eV]	LUMO [eV]	$E_g^{\text{CV}}$ [eV]	$T_{5\%}$ [°C]	$R$ [ $\Omega$ ]	$T_{\max}$ [°C]	Ref.
2-diMeTPA-1,3,4-ThdiAz	5000	301, 400	555	-5.16	-2.69	2.47	153	28.8	92	[22]
3,5-di(diMeTPA)-1,2,4-ThdiAz (or bTAThDaz)	5000	246, 300, 375	542	-5.19	-2.52	2.67	252	35.4	129	[22,23]
di-BenzThAz-terTh	5000	457	550	-5.07	-2.57	2.50	287	25.2	135	[22]
di(FPh-ThAz-An)-TPA (or PV-BLJ- SC11)	5000	295, 333, 385	nd	nd	nd	nd	145	33.7	130	[22,24]
PV-BLJ-SC9	900	424	nd	-5.20	-3.06	2.14	176	23.4	213	[26]
PV-BLJ-SC13	5000	insoluble	nd	-6.09	-3.91	2.18	390	113.8	43	[27]
PV-BLJ-SC14	5000	207, 246, 353, 444	496	-5.71	-3.33	2.38	294	102.4	40	[27]
PPL9	5000	295, 449	526	-5.41	-2.52	2.89	321	138.0	61	[25]

nd: not detected, CV: cyclic voltammetry, HOMO: highest occupied molecular orbital, LUMO: lowest unoccupied molecular orbital,  $R$ : resistance.



### di-BenzThAz-terTh

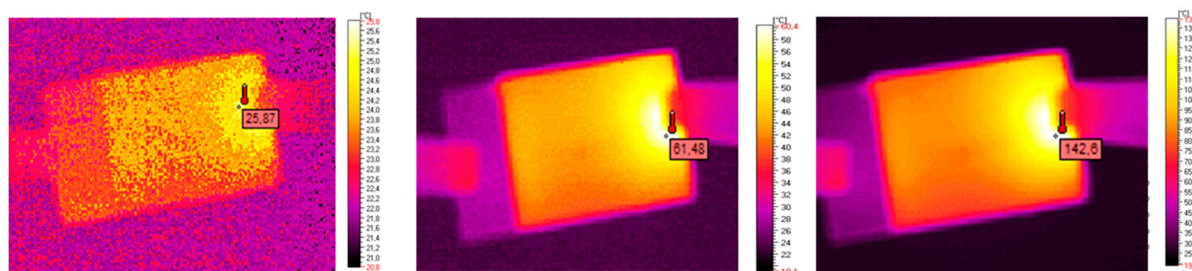


Fig. 4. Current-voltage and thermal-voltage curves of 8 investigated imines (a), and, as an example, thermal imaging for di-BenzThAz-terTh at 2 V, 6 V, and 10 V, from left (b). Reproduced from Ref. 22 with permission.

[Fig. 4(a), left], while a linear trend can be observed in the case of the flowing current. The analysis of thermal imaging in Refs. 22–27 allowed to present a heat map of the tested material as it can be seen in the exemplary image for di-BenzThAz-terTh [Fig. 4(b)].

The analysis of thermal imaging considers the voltage range, linking it with the results of the current flow. The correlation of such information does not allow to detect any structural defects but also suggests a possible origin, such as layer reorganization or thermal decomposition. Current-voltage curves of ITO/active layer/Ag/ITO are shown in Fig. 4(a). It can be seen that the current increases with the applied voltage increase and depends on the chemical structure of the investigated imines. The reorganization voltage of the devices was likely to occur above 6 V at temperatures above roughly 80 °C. It was very evident in the case of the PV-BLJ-SC9 (synthesized from 4-(thiophene-3-yl) aniline and 2,2':5',2''-terthiophene-5-carboxaldehyde), whereas in the case of other compounds only from temperature vs. voltage curve it is very difficult to observe a visible change.

For the purpose of this review, the evaluation of the influence of the sample temperature on current flow, resistance, conductivity, and thermal resistance is presented. At the core of understanding the heat generation due to the current flow is resistive (also called Joule) heating as the fundamental phenomena observed for inorganic and organic conductors and semiconductors [38–40]. The Joule heating power was calculated from the current flux distributions using the following equation:

$$G = I^2 \cdot \rho, \quad (1)$$

where  $G$ ,  $I$  and  $\rho$  stand for the heat (Joule heat power) [W/m<sup>3</sup>], the current density [A/m<sup>2</sup>], and the electrical resistivity [ $\Omega \cdot m$ ], respectively [41].

Firstly, the current values were plotted with the sample temperature to evaluate any possible inconsistency between both responses to the external potential. Since the current changes as the potential value increases, it is difficult to determine the exact influence of temperature on the passing current (see Fig. 5). As it was mentioned previously, a 3-minute interval was used within each individual potential value to ensure that any changes regarding evaluated voltage step were detected. All the samples resembled a similar nature of behaviour, namely an increment of the current value lining in an ascending order: PV-BLJ-SC9 > di(FPh-ThAz-An)-TPA (also PV-BLJ-SC11)  $\approx$  di-BenzThAz-terTh  $\approx$  2-diMeTPA-1,3,4-ThdiAz  $\approx$  3,5-di(diMeTPA)-1,2,4-ThdiAz > PV-BLJ-SC14 > PV-BLJ-SC13 > PPL9.

As a second one, a correlation between resistance and temperature was done. The graphical representation (Fig. 6) demonstrates a clear separation of behavioural patterns for each sample. The two symmetrical and asymmetrical imines based on 4-[4-(4-fluorophenyl)1,3-thiazol-2-yl]aniline and 2,2':5',2''-terthiophene-5,5''-dicarboxaldehyde or 2,2':5',2''-terthiophene-5-carboxaldehyde, PV-BLJ-SC13, PV-BLJ-SC14, respectively and PPL9 (obtained from 2-amino-5-(4-pyridyl)-1,3,4-thiadiazole and 4-(di-p-toliloamino)benzaldehyde) showed a decreasing resistance value upon changing temperature.

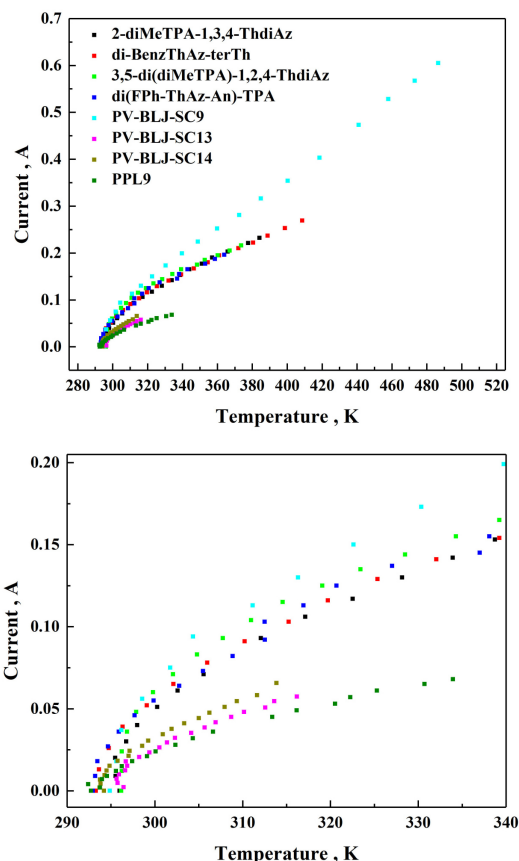


Fig. 5. Correlation between passing current and sample temperature for imines (full range: top, and inset for  $I_{max} = 0.20$  A and the maximum temperature of 340 K: bottom).

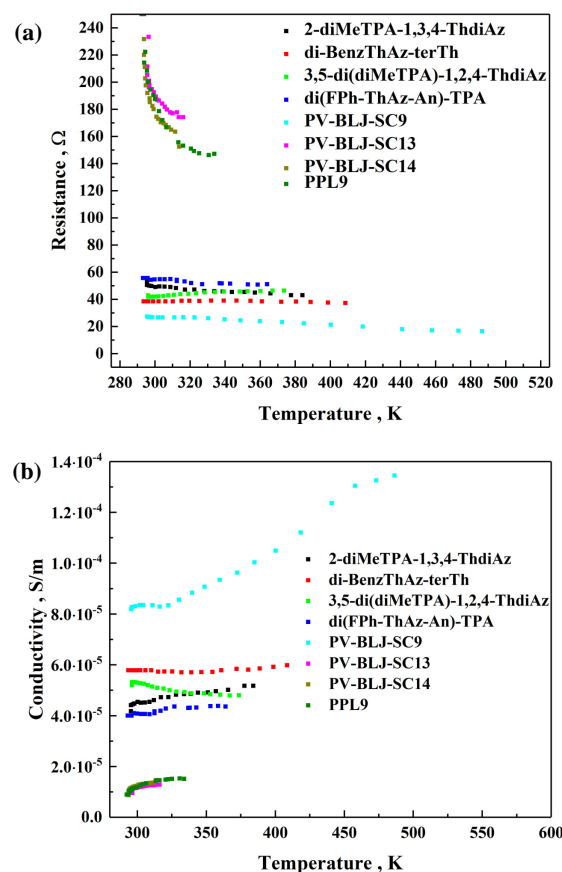


Fig. 6. Correlation between resistance (a) or conductivity (b) and sample temperature for imines.

Bearing in mind that among evaluated imines, these particular ones demonstrated poor solubility, polymerization [27], and showed in crystalline form [25], respectively suggests that the morphological rearrangement, or in the case of PV-BLJ-SC14, some polymerization reaction might take place, reducing the layer resistance. On the other hand, the remaining in this work 5 imines demonstrated a stable level or resistance over a wide temperature range. This might suggest that the layer formed by the spin coating technique results in an optimal rearrangement of molecules.

Evaluating the conductivity of layers composed of neat imines revealed that small changes in the resistance in the case of PV-BLJ-SC9 (synthesized from 4-(thiophene-3-yl)aniline and 2,2':5',2''-terthiophene-5-carboxaldehyde) have a great impact on the charge transfer, giving an improvement of almost 50% of starting conductivity [see Fig. 6(b)]. For other imines, di-BenzThAz-terTh, 3,5-di(diMeTPA)-1,2,3-ThdiAz, 2-diMeTPA-1,3,4-ThdiAz and di(FPh-ThAz-An)-TPA (see Fig. 2), the conductivity did not change significantly in a consequence of increasing temperature. The lowest conductivity was observed for PV-BLJ-SC13, PV-BLJ-SC14 imines (based on 4-[4-(4-fluorophenyl)1,3-thiazol-2-yl]aniline and 2,2':5',2''-terthiophene-5,5''-dicarboxaldehyde or 2,2':5',2''-terthiophene-5-carboxaldehyde, respectively) and PPL9 (obtained from 2-amino-5-(4-pyridyl)-1,3,4-thiadiazole and 4-(di-p-toliloamino)benzaldehyde), as it was expected taking resistance values evolution into account. The change of conductivity over increasing temperature could give the first inside information to explain the order of the sample molecules. Comparing the shape of the curves with Ref. 42 suggests that PV-BLJ-SC9, PV-BLJ-SC13, PV-BLJ-SC14, and PPL9 represent samples showing the mixt nature of the ordered-disordered alignment of molecules in the layer, whereas other imines displayed a very orderly alignment.

The analysis of thermal resistance and heat evolution as the temperature rises revealed only a small deviation of the results for all samples (Fig. 7). This might suggest that in the heat generation the ITO-coated glass has a significant impact, where the thin layers of the imine coating participate only to a small extend. These findings help to better understand the source of heat in the thermal images which is mostly the conducting substrate. Therefore, the imine coating conducts the heat generated below its layer, helping to indicate macroscopic defects created during sample preparation and confirms that the electric behaviour of layers changes mainly due to “external heating” rather than self-heating during the current flow through the layer.

Concluding this section, the thermoelectric studies can reveal much more information about imines thin layers than the values of thermal resistance, thermal and electrical resistance, or conductivity values. The evolution of these parameters in the temperature range provides information about molecular changes occurring in the layer such as the reorganization or decomposition of molecules. Given the molecular structure, PV-BLJ-SC9 seems to be the best candidate to be used in the solar cell application due to its planar structure and possibility to polymerize via thiophene unit at both ends.

Furthermore, the identical end sides might facilitate the  $\pi$ - $\pi$  interactions, hence forming a molecular polymer with a conjugated structure of the monomer. Additionally, this

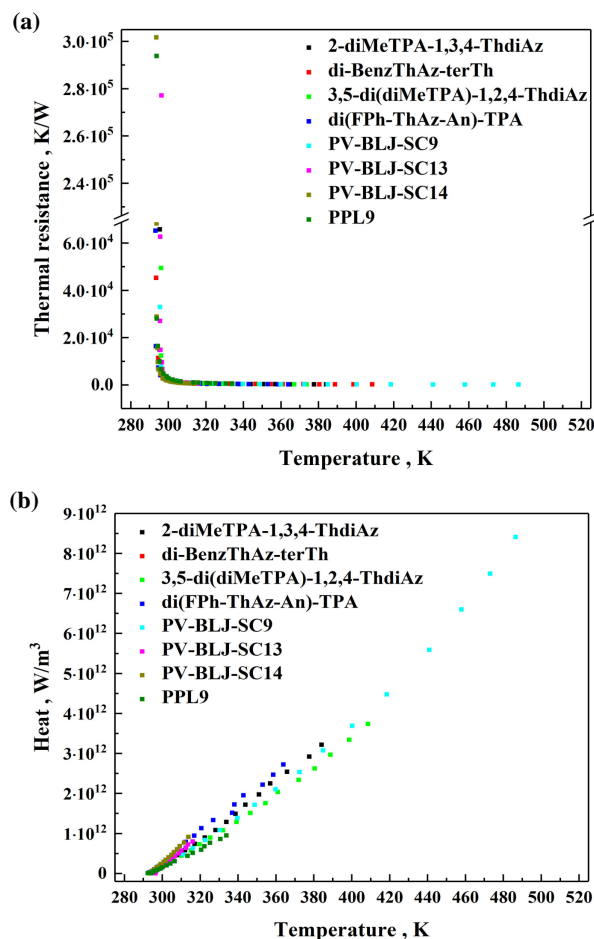


Fig. 7. Correlation between thermal resistance (a) or heat (b) and sample temperature for imines.

imine gave one of the lowest resistance values around 23  $\Omega$  and the highest conductivity ranging between  $8.0 \cdot 10^{-5}$  S/m to  $1.35 \cdot 10^{-5}$  S/m. Another imine, that possesses similar molecular structure and slightly lower thermoelectric properties was di-BenzThAz-terTh (synthesized from 2,2':5',2''-terthiophene-5,5''-dicarboxaldehyde and 2-aminobenzothiazole); benzothiazole terminal unit should form  $\pi$ - $\pi$  interactions forming molecular polymers, as well. Comparison of resistivity ( $R$ ) and temperature of heating ( $T_{max}$ ) is presented schematically for all investigated imines in Fig. 8.

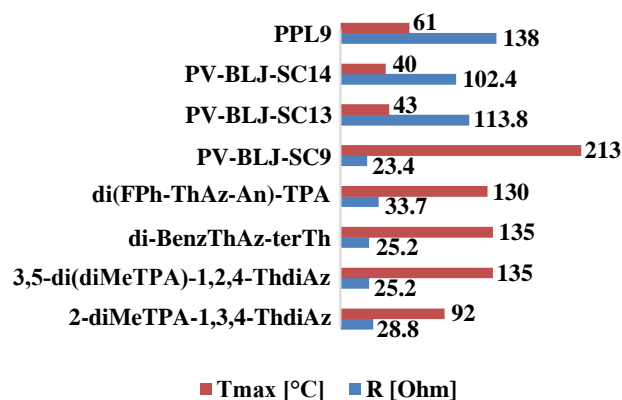


Fig. 8. Comparison of resistivity ( $R$ ) and temperature of heating ( $T_{max}$ ) of investigated imines.

#### 4. Thermoelectrical properties of doped imines

In this article, multicomponent layers containing above mentioned eight imines with different molecular structures were selected. As other component of the organic layer, poly[[4,8-bis[(2-ethylhexyl)oxy]benzo[1,2-b:4,5-0]dithiophene-2,6-diyl][3-fluoro-2-[(2-ethylhexyl)carbonyl]thieno 3,4-b]thiophenediyl]] (PTB7) and phenyl-C<sub>70</sub>-butyric acid methyl ester (PC<sub>71</sub>BM) or camforsulphonic acid (CSA) were used in different proportions. Selected properties of these multicomponent mixtures containing imines can be found in Table 2.

The architecture of the device containing a multicomponent layer did not differ from the one used for a neat imines layer and also had the ITO/active layer/Ag/ITO architecture. The representation of thermal

Table 2.

Summary of electrical and thermal properties of selected imines and their multicomponent mixtures.

Code	spin speed [rpm]	R [Ω]	T <sub>max</sub> [°C]	Ref.
2-diMeTPA-1,3,4-ThdiAz	5000	28.8	92	[21]
2-diMeTPA-1,3,4-ThdiAz:PTB7 (0.7:1)	5000	51.3	54	[21]
3,5-di(diMeTPA)-1,2,4-ThdiAz (or bTAThDaz)	5000	25.2	135	[21,22]
3,5-di(diMeTPA)-1,2,4-ThdiAz:PTB7 (0.3:1)	5000	21.3	143	[21]
di-BenzThAz-terTh	5000	25.2	135	[21]
di-BenzThAz-terTh:PTB7 (0.4:1)	5000	25.1	125	[21]
di(FPh-ThAz-An)-TPA (or PV-BLJ- SC11)	5000	33.7	130	[21,23]
di(FPh-ThAz-An)-TPA:PTB7 (0.4:1)	5000	23.0	92	[21]
PV-BLJ-SC9	900	23.4	213	[24]
PV-BLJ-SC9:PTB7 (1:4)	900	26.1	268*	[24]
PV-BLJ-SC9:PC <sub>71</sub> BM (1:8)	900	25.4	186*	[24]
PV-BLJ-SC9:PTB7:PC <sub>71</sub> BM (1:4:8)	900	23.1	236	[24]
PV-BLJ-SC9:PTB7 (1:8)	900	18.3	237*	[24]
PV-BLJ-SC9:PC <sub>71</sub> BM (1:13)	900	19.1	225*	[24]
PV-BLJ-SC9:PTB7:PC <sub>71</sub> BM (1:8:13)	900	20.5	204	[24]
PV-BLJ-SC11	5000	28.2	92	[24]
PV-BLJ-SC11:PTB7 (1:1)	5000	32.2	48	[23]
PV-BLJ-SC11:PC <sub>71</sub> BM (1:1)	5000	43.2	95	[23]
PV-BLJ-SC13	5000	113.8	43	[25]
PV-BLJ-SC13:PTB7 (1:1)	5000	91.5	52	[25]
PV-BLJ-SC13:PC <sub>71</sub> BM (1:1)	5000	96.2	48	[25]
PV-BLJ-SC14	5000	102.4	40	[25]
PV-BLJ-SC14:PTB7 (1:1)	5000	84.6	57	[25]
PV-BLJ-SC14:PC <sub>71</sub> BM (1:1)	5000	101.0	43	[25]
PPL9	5000	138.0	61	[26]
PPL9:CSA(+) (1:1)	5000	139.0	48	[26]

\* means decomposition of the sample above 8 V.

and electrical properties was analogous to the one presented for layers made of imine alone. The addition of PTB7 improved in general the electric parameters of the layer, whereas the PC<sub>71</sub>BM caused a decrease of internal resistance compared to imine. As for the CSA, this did not affect the current flow, however, it reduced the registered temperature of the sample. For the binary composition, a decomposition of samples was observed for some cases, resulting in a decrease of the current flow. The heat maps of binary and ternary compositions were more homogenous than for neat imine layers [22–27].

As for neat imine layers, current values of the multicomponent layers were plotted with the sample temperature to evaluate any possible inconsistency between both responses to the external potential (Fig. 9). As with neat imine, it is difficult to approximate whereas the change of the current due to applied external voltage is affected by the change of the temperature. All the samples resembled a similar nature of behaviour, slightly higher than neat imine in the same increasing order as pure imines.

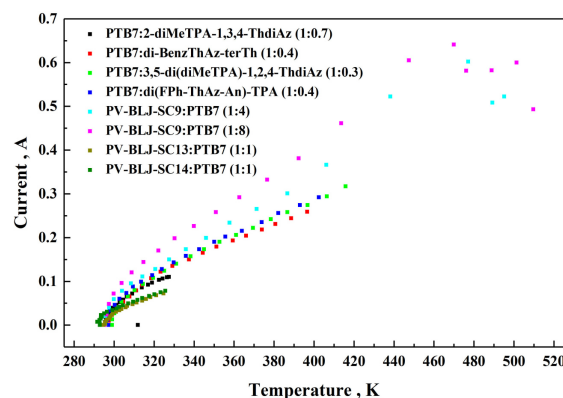


Fig. 9. Correlation between passing current and sample temperature for PTB7:imines, as an example.

The correlation between resistance and temperature was done for binary and ternary compositions. The graphical representation (Fig. 10) demonstrates a clear separation of behavioural patterns for each sample. The samples containing PV-BLJ-SC13 and PV-BLJ-SC14 from both PTB7 and PC<sub>71</sub>BM, some small changes have been observed. Generally, the presence of PTB7 improves conductivity of imine up to 20% of the starting value. Only in the case of 2-diMeTPA-1,3,4-ThdiAz (obtained from 4-(ditolylamino)benzaldehyde and 2-amino-1,3,4-thiadiazole) a drastic decline in the overall electric performance was observed; the resistance has increased of about half of the value for pure imine, causing a decrease of conductivity. In the case of binary compositions of PV-BLJ-SC9, a decline in performance was observed at higher temperatures due to a possible decomposition of the compound. In all other cases, binary and ternary compositions possessed probably much better organization of molecules in the layer; the confirmation can be found in the shape of resistance and conductivity curves, namely in a steady behaviour regardless of the temperature increment compared with Ref. 42.

The analysis of thermal resistance and heat evolution relative to rising temperature for multicomponent layers revealed some small deviation of the results for all samples (Fig. 11). This might suggest that in the heat generation the ITO-coated glass has a significant impact, however, in cases of higher electrical resistance, the bending of the thermal

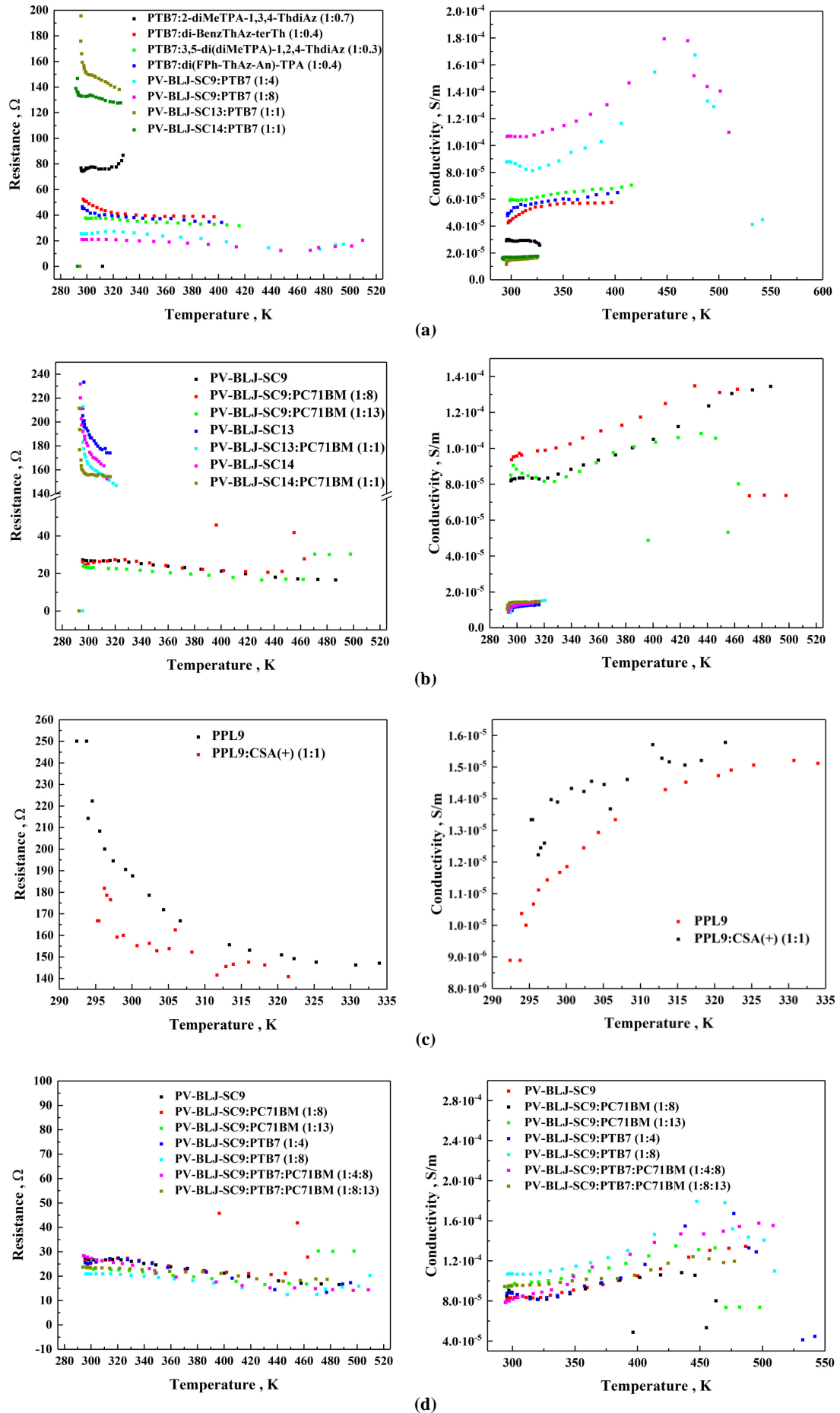


Fig. 10. Correlation between resistance (left side) or conductivity (right side) and sample temperature for binary systems with PTB7 (a), PC<sub>71</sub>BM (b, c) and CSA (c), and comparison of binary and ternary samples with PV-BLJ-SC9 imine (d).



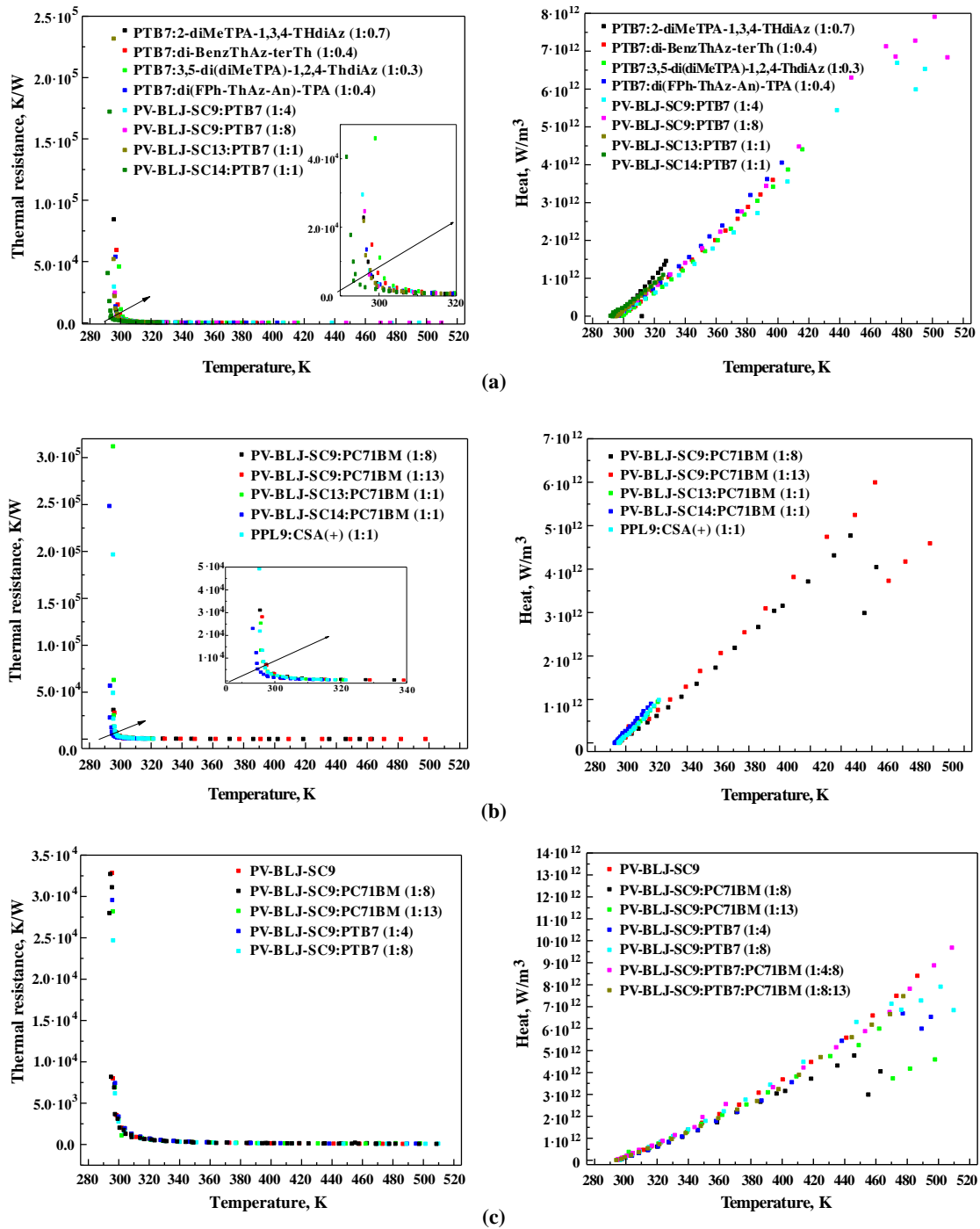


Fig. 11. Correlation between thermal resistance (left side) or heat (right side) and sample temperature for imines in undoped and doped state: for binary systems with PTB7 (a), PC<sub>71</sub>BM or CSA (b), and comparison of binary and ternary samples with PV-BLJ-SC9 imine (c).

resistance curve has been shifted toward higher temperatures. It might suggest that the whole device has some thermal capacity that needs to be reached to conduct the heat outside. However, the general conclusions that the imine coating conducts heat generated below its layer, helping to indicate macroscopic defects is still valid.

To summarize the section dedicated to multicomponent compositions, it is possible to follow the changes in the thermoelectric parameters giving enriched information about the layers. This technique also showed high sensitivity to the change in a composition of the tested mixture proving it diagnostic meaning. Moreover, thermal evolution of thermal resistance, thermal and electrical resistance, or conductivity values inform about molecular

changes occurring in the layer like reorganization of molecules or their decomposition. Also, in the case of binary and ternary compositions, the best results were obtained for a composition containing PV-BLJ-SC9 (synthesized from 4-(thiophene-3-yl)aniline and 2,2':5',2''-terthiophene-5-carboxaldehyde) in terms of all thermoelectric properties. The mixed compositions with this imine showed improvement of almost all parameters up to 10% of the value reported for the neat imine. In the case of di-BenzThAz-terTh (synthesized from 2,2':5',2''-terthiophene-5,5''-dicarboxaldehyde and 2-aminobenzothiazole), it did not show any improvement in terms of thermoelectric properties. It means that multicomponent compositions do not possess boosted values of conductivity.

## 5. Summary of the results and their link to photovoltaic parameters

In this article eight imine and their binary or ternary compositions with PTB7, PC<sub>71</sub>BM or CSA were analysed for the heat effect on thermoelectric properties using the coupled technique. The coupled thermal imaging and chronoamperometry techniques provide a wide range of information about the sample and its electric properties and enable the thermal mapping of defects. Additional analyses presented in this work gave even more input about: participation of the sample in the overall heating generation (thermal resistance and Joule heat power) and influence of increasing temperature on electrical resistance and conductivity. The shape of conductivity curve in relation to temperature changes might suggest the orientation state of molecules in a formed layer allowing the approximation of molecules in the layer that are highly oriented, mixed oriented-unoriented, or highly unoriented. From the thermoelectric properties assessment, PV-BLJ-SC9 demonstrated the most promising results for neat imine, binary and ternary compositions for potential use in organic photovoltaics.

Only for three evaluated imines: PV-BLJ-SC9, PV-BLJ-SC13 and PV-BLJ-SC14, the results for constructed organic solar cells are available in Refs. 23 and 25 and main photovoltaic parameters are displayed in Table 3. The best parameters were obtained for PV-BLJ-SC9, the power conversion efficiency (PCE) was equal to 4%, whereas for other two the PCE were found below 0.42%. From the performed analysis of thermoelectric properties, PV-BLJ-SC9 showed a predisposition for such application. On the other hand, PV-BLJ-SC13 and PV-BLJ-SC14 were found not perspective due to high resistance, low conductivity, and insignificant improvement of those properties in binary compositions. These findings confirm that thermal imaging coupled with chronoamperometry could be a useful tool together with other traditional characterization techniques to perform a screening for a new organic compound for

organic solar cells. IR images obtained for the constructed devices based on PV-BLJ-SC9 and their binary and ternary compositions at 2 V, 6 V, and 10 V are presented in Fig. 12.

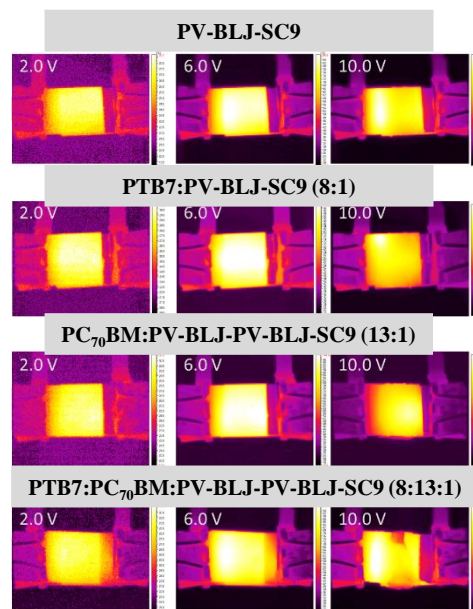
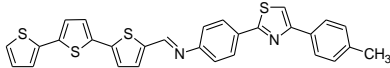
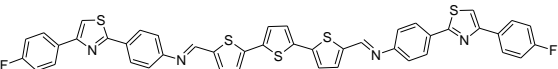
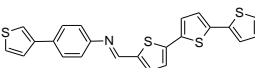


Fig. 12. IR images obtained for constructed devices based on PV-BLJ-SC9 and their binary and ternary compositions at 2 V, 6 V, and 10 V.

Finally, it can be emphasized that the analysis of compounds or mixtures using a thermal imaging camera coupled with chronoamperometry allows to reduce the costs associated with the construction of organic solar cells by initially eliminating compounds that do not meet the electrical, thermal, and structural requirements for active or hole transporting layers. Thus, the proposed coupled technique is part of the latest research and social trend related to the aspects of Green Chemistry and global warming by reducing the number of materials used, the source of which, as well as other products, is crude oil.

Table 3.

Photovoltaic parameters of the selected devices containing imines, where:  $V_{oc}$  is the open circuit voltage,  $J_{sc}$  is the short circuit current, FF is the fill factor, PCE is the power conversion efficiency, and PEDOT:PSS is poly(3,4-ethylenedioxythiophene):poly(styrenesulfonate).

Chemical structure of imine/ architecture of solar cell	$V_{oc}$ , [V]	$J_{sc}$ , [mA/cm <sup>2</sup> ]	FF, -	PCE, [%]	Ref.
	0.75	0.60	0.13	0.06	[25]
ITO/PEDOT:PSS/PTB7: <b>PV-BLJ-SC14</b> :PC <sub>71</sub> BM (8:1:13)/Al					
	0.67	1.60	0.39	0.42	[25]
ITO/PEDOT:PSS/PTB7: <b>PV-BLJ-SC13</b> :PC <sub>71</sub> BM (4:1:8)/Al					
	0.72	10.9	0.52	4.0	[23]
ITO/PEDOT:PSS/PTB7: <b>PV-BLJ-SC9</b> :PC <sub>71</sub> BM (8:1:13)/In/Al					

## Acknowledgements

The experimental results were obtained from the projects funded by The Polish National Centre of Research and Development (TECHMATSTRATEG1/347431/14/NCBR/2018) for such compounds as di-BenzThAz-terTh, di(FPh-ThAz-An)-TPA, PV-BLJ-SC13 and PV-BLJ-SC14, and project No. V4-Korea/1/2018 for compounds 3,5-di(diMeTPA)-1,2,4-ThdiAz, 2-diMeTPA-1,3,4-ThdiAz and PPL9.

## References

- [1] Wang, D. *et al.* Recent advances in molecular design of organic thermoelectric materials. *CCS Chem.* **3**, 2212–2225 (2021). <https://doi.org/10.31635/ccschem.021.202101076>
- [2] Dong, J. *et al.* Organic semiconductor nanostructures: Optoelectronic properties, Modification strategy, and photocatalytic applications. *J Mater. Sci. Tech.* (2021). <https://doi.org/10.1016/j.jmst.2021.09.002>
- [3] Huang, D. *et al.* Conjugated-backbone effect of organic small molecules for n-type thermoelectric materials with ZT over 0.2. *J. Am. Chem. Soc.* **139**, 13013–13023 (2017). <https://doi.org/10.1021/jacs.7b05344>
- [4] Mao, L. *et al.* Patching defects in the active layer of large-area organic solar cells. *J. Mater. Chem. A* **6**, 5817–5824 (2018). <https://doi.org/10.1039/C7TA11264E>
- [5] Lindner, S. M. *et al.* Charge separation at self-assembled nanostructured bulk interface in block copolymers. *Angew. Chem* **45**, 3364–3368 (2006). <https://doi.org/10.1002/anie.200503958>
- [6] Han, Y. *et al.* Calibration and image processing of aerial thermal image for UAV application in crop water stress estimation. *J. Sensors* **2021**, Article ID 5537795 (2021). <https://doi.org/10.1155/2021/5537795>
- [7] Stumper, M., Kraus, J. & Capousek, L. Thermal imaging in aviation. *Magazine of Aviation Development* **3**, 16 (2015). <https://doi.org/10.14311/MAD.2015.16.03>
- [8] Thermal Imaging in the Automotive Industry. *Thermascan Ltd* <https://www.thermascan.co.uk/blog/thermal-imaging-automotive> (2021).
- [9] Thermography in Chemical Industry. *InfraTec GmbH* <https://www.infratec.eu/thermography/industries-applications/chemical-industry/> (2021).
- [10] Kasikowski, R. & Wiecek, B. Fringing-effect losses in inductors by thermal modeling and thermographic measurements. *IEEE Trans. Power Electron.* **36**, 9772–9786 (2021). <https://doi.org/10.1109/TPEL.2021.3058961>
- [11] Kucharska, M. & Jaskowska-Lemanska, J. Active thermography in diagnostics of timber elements covered with polychrome. *Materials* **14**, 1134 (2021). <https://doi.org/10.3390/ma14051134>
- [12] Kowalski, M. Ł., Grudzień, A. & Ciurapiński, W. Detection of human faces in thermal infrared images. *Metrolog. Meas. Syst.* **28**, 307–321 (2021). <https://doi.org/10.24425/mms.2021.136609>
- [13] Teubner, J. *et al.* Comparison of drone-based ir-imaging with module resolved monitoring power data. *Energy Procedia* **124**, 560–566 (2017). <https://doi.org/10.1016/j.egypro.2017.09.094>
- [14] Irshad, Jaffery, Z. A. & Haque, A. Temperature measurement of solar module in outdoor operating conditions using thermal imaging. *Infrared Phys. Technol.* **92**, 134–138 (2018). <https://doi.org/10.1016/j.infrared.2018.05.017>
- [15] Gallardo-Saavedra, S. *et al.* Infrared thermography for the detection and characterization of photovoltaic defects: comparison between illumination and dark conditions. *Sensors* **20**, 4395 (2020). <https://doi.org/10.3390/s20164395>
- [16] Mutillo, M. *et al.* On field infrared thermography sensing for pv system efficiency assessment: results and comparison with electrical models. *Sensors* **20**, 1055 (2020). <https://doi.org/10.3390/s20041055>
- [17] Iwan, A. *et al.* Optical and electrical properties of graphene oxide and reduced graphene oxide films deposited onto glass and Ecoflex® substrates towards organic solar cells. *Adv. Mater. Lett* **9**, 58–65 (2018). <https://doi.org/10.5185/amlett.2018.1870>
- [18] Fryń, P. *et al.* Hybrid materials based on 1,d-poly(lactic acid) and single-walled carbon nanotubes as flexible substrate for organic devices. *Polymers* **10**, 1271 (2018). <https://doi.org/10.3390/polym10111271>
- [19] Fryń, P. *et al.* Dielectric, thermal and mechanical properties of L,D-Poly(Lactic Acid) modified by 4'-Pentyl-4-Biphenylcarbonitrile and single walled carbon nanotube. *Polymers* **11**, 1867 (2019). <https://doi.org/10.3390/polym11111867>
- [20] Fryń, P. *et al.* Research of binary and ternary composites based on selected aliphatic or aliphatic–aromatic polymers, 5CB or SWCN toward biodegradable electrodes. *Materials* **13**, 2480 (2020). <https://doi.org/10.3390/ma13112480>
- [21] Różycka, A. *et al.* Influence of TiO<sub>2</sub> nanoparticles on liquid crystalline, structural and electrochemical properties of (8Z)-N-(4-(Z)-(4-pentylphenylimino)methyl)benzylidene)-4-pentylbenzenamine. *Materials* **12**, 1097 (2019). <https://doi.org/10.3390/ma12071097>
- [22] Gonciarz, A. *et al.* UV-Vis absorption properties of new aromatic imines and their compositions with poly([4,8-bis(2-ethylhexyl)oxy]benzo[1,2-b:4,5-b']dithiophene-2,6-diyl){3-fluoro-2-[(2-ethylhexyl)carbonyl]thieno[3,4-b]thiophenediyl}. *Materials* **12**, 4191 (2019). <https://doi.org/10.3390/ma12244191>
- [23] Bogdanowicz, K. A. Selected electrochemical properties of 4,4'-(1E,1'E)-((1,2,4-thiadiazole-3,5-diyl)bis(azaneylylidene))bis-(methaneylylidene)bis(N,N-di-p-tolylaniline) towards perovskite solar cells with 14.4% efficiency. *Materials* **13**, 2440 (2020). <https://doi.org/10.3390/ma13112440>
- [24] Przybył, W. *et al.* IR thermographic camera as useful and smart tool to analyse defects in organic solar cells. *Photonics Lett. Poland* **12**, 25–27 (2020). <https://doi.org/10.4302/plp.v12i2.976>
- [25] Jewloszewicz, B. *et al.* A comprehensive optical and electrical study of unsymmetrical imine with four thiophene rings and their binary and ternary compositions with PTB7 and PC70BM towards organic photovoltaics. *RSC Adv* **10**, 44958 (2020). <https://doi.org/10.1039/D0RA08330E>
- [26] Bogdanowicz, K. A. *et al.* Electrochemical and optical studies of new symmetrical and unsymmetrical imines with thiazole and thiophene moieties. *Electrochim Acta* **332**, 135476 (2020). <https://doi.org/10.1016/j.electacta.2019.135476>
- [27] Dylong, A. *et al.* Crystal structure determination of 4-[(Di-p-tolylamino)-benzylidene]-(5-pyridin-4-yl-[1,3,4]thiadiazol-2-yl)-imine along with selected properties of imine in neutral and protonated form with camforosulphonic acid: Theoretical and experimental studies. *Materials* **14**, 1952 (2021). <https://doi.org/10.3390/ma14081952>
- [28] Wang, J. *et al.* Stimulus responsive fluorescent hyperbranched polymers and their applications. *Sci. China Chem.* **53**, 2409–2428 (2010). <https://doi.org/10.1007/s11426-010-4106-9>
- [29] Albota, A. *et al.* Design of organic molecules with large two-photon absorption cross sections. *Science* **281**, 1653 (1998). <https://doi.org/10.1126/science.281.5383.1653>
- [30] Reinhardt, B. A. *et al.* Highly active two-photon dyes: design, synthesis, and characterization toward application. *Chem. Mater.* **10**, 1863 (1998). <https://doi.org/10.1021/cm980036e>
- [31] Iwase, Y. *et al.* Synthesis and photophysical properties of new two-photon absorption chromophores containing a diacetylene moiety as the central  $\pi$ -bridge. *J. Mater. Chem.* **13**, 1575 (2000). <https://doi.org/10.1039/b211268j>
- [32] Kim, O. K. *et al.* New class of two-photon-absorbing chromophores based on dithienothiophene. *Chem. Mater.* **12**, 284 (2000). <https://doi.org/10.1021/cm990662r>
- [33] Liu, Z. Q. *et al.* Trivalent boron as an acceptor in donor– $\pi$ –acceptor-type compounds for single- and two-photon excited fluorescence. *Chem. Eur. J.* **9**, 5074 (2003). <https://doi.org/10.1002/chem.200304833>
- [34] Abbotto, A. *et al.* Novel heterocycle-based two-photon absorbing dyes. *Org. Lett.* **4**, 1495 (2002). <https://doi.org/10.1021/ol025703v>
- [35] Sek, D. *et al.* Hole transport triphenylamine-azomethine conjugated system: Synthesis and optical, photoluminescence and electrochemical properties. *Macromolecules* **41**, 6653–6663 (2008). <https://doi.org/10.1021/ma702637k>
- [36] Sek, D. *et al.* Characterization and optical properties of oligoazomethines with triphenylamine moieties exhibiting blue, blue-green and green light. *Spectrochim Acta A Mol. Biomol. Spectrosc.* **72**, 1–10 (2009). <https://doi.org/10.1016/j.saa.2008.06.022>
- [37] Gawlinska, K. *et al.* Searching of new, cheap, air- and thermally stable hole transporting materials for perovskite solar cells. *Opto-*

- Electron. Rev.* **25**, 274–284, (2017).  
<https://doi.org/10.1016/j.opelre.2017.07.004>
- [38] Costa, P. M. J. F. *et al.* Direct imaging of Joule heating dynamics and temperature profiling inside a carbon nanotube interconnect. *Nat. Commun.* **2**, 421 (2011). <https://doi.org/10.1038/ncomms1429>
- [39] McLaren, C. T. *et al.* Development of highly inhomogeneous temperature profile within electrically heated alkali silicate glasses. *Sci. Rep.* **9**, 2805 (2019). <https://doi.org/10.1038/s41598-019-39431-8>
- [40] Balakrishnan, V. *et al.* A generalized analytical model for Joule heating of segmented wires. *J. Heat Transfer* **140**, (7), 072001 (2018). <https://doi.org/10.1115/1.4038829>
- [41] Thangaraju, S. K. & Munisamy, K. M. Electrical and Joule Heating Relationship Investigation Using Finite Element Method. in *7th International Conference on Cooling & Heating Technologies*. **88**, 012036 (Selangor, Malaysia, 2015).  
<https://doi.org/10.1088/1757-899X/88/1/012036>
- [42] Russ, B. *et al.* Organic thermoelectric materials for energy harvesting and temperature control. *Nat. Rev. Mater.* **1**, 16050 (2016). <https://doi.org/10.1038/natrevmats.2016.50>